Low-Bias Terahertz Amplitude Modulator Based on Split-Ring Resonators and Graphene

Riccardo Degl'Innocenti,[†,*] David S. Jessop,[†] Yash D. Shah,[†] Juraj Sibik,[‡] J. Axel Zeitler,[‡] Piran R. Kidambi,[§] Stephan Hofmann,[§] Harvey E. Beere,[†] and David A. Ritchie[†]

[†]Cavendish Laboratory, University of Cambridge, J. J. Thomson Avenue, Cambridge CB3 0HE, United Kingdom, [‡]Department of Chemical Engineering and Biotechnology, University of Cambridge, J. J. Thomson Avenue, Cambridge CB3 0HE, United Kingdom, and [§]Department of Engineering, University of Cambridge, J. J. Thomson Avenue, Cambridge CB3 0FA, United Kingdom

ABSTRACT Split-ring resonators represent the ideal route to achieve optical control of the incident light at THz frequencies. These subwavelength metamaterial elements exhibit broad resonances that can be easily tuned lithographically. We have realized a design based on the interplay between the resonances of metallic split rings and the electronic properties of monolayer graphene integrated in a single device. By varying the major carrier concentration of graphene, an active modulation of the optical intensity was achieved in the frequency range between 2.2 and 3.1 THz, achieving a maximum modulation depth of 18%, with a bias as low as 0.5 V.

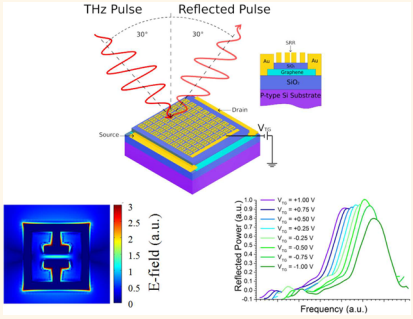

KEYWORDS: terahertz · graphene · metamaterial · optical modulator · time-domain spectroscopy · optoelectronics

Active optical modulators working in the terahertz (THz) region represent a key element for many applications continuously developing in this frequency range such as sensing, optical communications, and security scanning.[1,2] State of the art THz technology spans a diverse range, from methods for generating broadband radiation used in the time-domain-spectroscopy (TDS) field to complementary, compact solid state lasers such as quantum cascade lasers (QCLs). All these different research areas require fast, compact, and active amplitude/phase modulators as well as fast detectors in order to exploit their full potential. Moreover, the integration of devices that are capable of manipulating THz radiation with QCL sources is a key requirement for active control applications, such as beam steering or frequency locking. Metamaterials, such as split-ring resonators (SRR), offer the possibility to design and manipulate the electromagnetic properties of the materials, thus compensating for their poor response in this frequency range. Split-ring arrays, yielding broad resonances that can be easily tuned in frequency by varying their dimensions, have already been successfully employed in the THz range.[3−5] By biasing metallic split rings with respect to an n^+ GaAs substrate, an amplitude/phase modulation was achieved at THz frequencies.

Here, we develop this concept further, by introducing a graphene monolayer, integrated below the split ring array in the device architecture. There is a vast literature regarding graphene and its peculiar electronic properties, described in detail elsewhere.[6−8] Due to the high confinement that can be achieved in graphene,[9−12] this material is of particular interest in the field of plasmonics.[13] This opens up new opportunities in fast modulation and, together with the greater ease of tuning the material properties over conventional semiconductor material, makes graphene an ideal candidate for designing optoelectronic devices in the THz frequency range. Lately, the possibility of using graphene as the key element in active/passive THz optical modulators and optoelectronic devices has been reported in several articles. The experiments

* Address correspondence to rd448@cam.ac.uk.

Received for review November 28, 2013 and accepted February 13, 2014.

Published online February 13, 2014
10.1021/nn406136c

presented in refs 14 and 15 are based on an architecture similar to a Fabry–Perot cavity, where the modulation of the graphene sheet conductivity results in a change of the optical absorption/reflection of the device. This approach yields a high modulation depth (64%), but it is not optimal in efficient voltage modulation, since it requires a 30 V bias. Furthermore, such a high modulation depth is obtained by acting on the total device thickness, which being fixed cannot support modulation of different frequencies at the same time. The implementation of metamaterial elements capable of enhancing the interaction between a graphene layer and the resonances artificially engineered on top of the material has proven to be a further step toward the integration of such hybrid devices for the realization of a compact, room-temperature, fast, tunable optical modulation.[16,17] A modulator device based on metamaterial (SRR) and graphene has been recently realized[18] reporting a modulation depth of 11.5%, corresponding to an applied bias of 10.6 V. Here we provide a more flexible approach to tunability, due to the integration of different frequency-independent resonant arrays and a more efficient voltage modulation, due to the implementation of a top-gated architecture than in this reported work.

A top-gate architecture can readily realize an integrated device that could easily be employed as an amplitude/phase modulator in a selective frequency range, based on the interplay between split-ring arrays and a graphene monolayer, where the bias is applied through the split rings themselves, thus acting as top gate. This results in a higher maximum modulation depth, of about 18%, with a much lower bias voltage of less than 1 V, an order of magnitude smaller than the results presented in refs 14 and 18. Furthermore, it is important to stress that the implementation of the conventional bottom gate by using the p^+ Si-substrate, for setting the working point, and of a top gate, for modulation, paves the way to the realization of an efficient detection and/or imaging system, based on the interplay between graphene and metamaterial resonances. Since we also target the realization of optical modulation of THz QCLs, we designed our device with multiple, independently biased resonances, spanning the favorable frequency range for QCLs between 2 and 3 THz. We tested our system with a THz-TDS system based on photoconductive antennas, and the broad and evident resonances were tuned by acting on the doping level of the graphene layer.

RESULTS AND DISCUSSION

A schematic of the final device is presented in Figure 1a, with the fabrication details reported in the

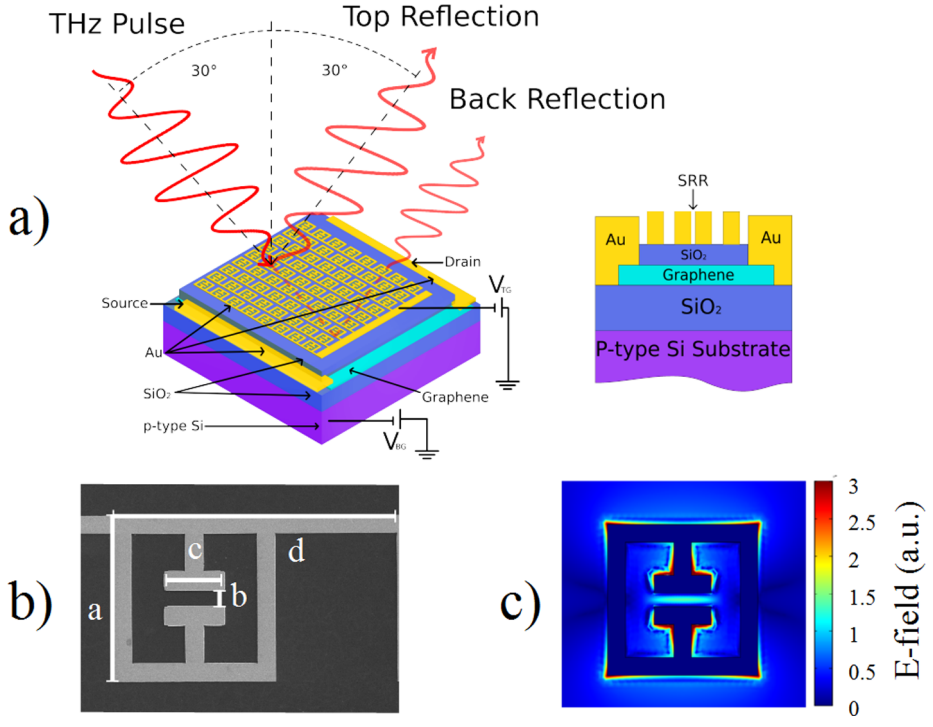

Figure 1. Schematic diagram of a split-ring array coupled to graphene with a SiO_2 buffering layer. The graphene monolayer is deposited *via* CVD on top of a Si/SiO_2 chip. Graphene arrays with an area of 1 mm^2 each were defined by using optical lithography and oxygen plasma etching. A 35 nm oxide buffering layer separates the graphene from the metal SRR. The split rings, which are all contacted, are then defined by e-beam lithography, Ti/Au 10/80 nm deposition, and lift off. (a) We monitored the reflected power from the top and back sample surfaces at different bias VTG of the split-ring arrays with respect to the graphene monolayer. (b) Scanning electron microscope picture of an SRR: the metal width ratio to SRR side length *a* was kept fixed at 0.1; the *d/a*, *c/a*, and *b/a* ratios were 1.75, 0.36, and 0.10, respectively. The side *a* varied among the different arrays, assuming the values of 20, 22, 24, and 26 μm. (c) Simulation of the split-ring resonance done using the commercial software Comsol Multiphysics. The LC resonance presents maximum *E*-field enhancement in the capacitor gap in resonance.

Methods section. The split-ring arrays were designed such that the resonances could continuously match the spectral range covered by QCL emission, between 2 and 3 THz. The split-ring dimensions were varied among the different arrays, in order to achieve a spacing in frequency of the individual resonances of about 250 GHz from 2.2 THz to 3.1 THz. Particularly, the resonator dimensions, normalized to the side *a* (a scanning electron microscope picture of a SRR, together with the main fabrication parameters, is presented in Figure 1b), were kept fixed among the different arrays while the SRR side length assumed the values 20−22−24−26 μm, corresponding to a frequency of 3.1−2.75−2.5−2.2 THz, respectively. Our target is the LC resonance, arising from the coupling of the inductance, which is given by the arms of the SRR, and the capacitance, which is mainly determined by the split gap (*b*). This resonance, which is excited by a component of the incident THz *E*-field perpendicular to the capacitor element, has a maximum power concentration in the gap, as calculated by Comsol Multiphysics v. 4.3 and shown in Figure 1c.

Measurements and Simulations. The first step involved the characterization of the patterned graphene area. The resistance between source and drain was monitored at different back-gate biases, using Keithley voltage sources (models 2400 and 236), while the top-gate was kept unbiased. The current passing through the source and drain pads was kept below 10 μA. The results, as shown in Figure 2 for the array with a = 22 μm, present the charge neutrality point (CNP) for negative biases around −6 V. It is remarkable that similar values are also shown by the other split-ring arrays, exhibiting CNPs between −6 and −4 V, consistently reproducible after months. The CNP along with the SiO_2 thickness and permittivity allowed us to work out the zero-bias doping density, using a standard parallel plate capacitor model. This was found to vary between 2.8 × 10^{11} and 4.3 × 10^{11} cm^{-2}, assuming 3.85 for the relative dielectric constant of the SiO_2 layer and 300 nm for its thickness. A negative CNP is compatible with n-doped graphene. This shift from the expected p-doping of the CVD graphene was attributed to both the interaction between the graphene sheet and the Ti metal of the pads[19] and the thermal curing of FOX-2 resist.[20] The consistent reproducibility of the CNP value can be attributed to the buffer layer preventing any significant addition of charge impurities. The devices were tested with a commercially available THz pulsed imaging system, Imaga 2000 from Teraview (Cambridge, UK), based on biased photoconductive antennas.[21] The sample was illuminated by a focused spot size of about 200 μm^2 at an incidence angle of 30° to the normal. The reflected light from the split-ring arrays was monitored at different back-gate biases with the polarization fixed along the split-ring gap. The reflected electric field was recorded at different spatial coordinates with a step size of 100 μm, by keeping the SRR arrays always in the focus of the TDS system. Figure 3 presents the maximum reflected *E*-field registered at different positions of the 2 × 2 array in the sample, thus yielding a THz map of the whole device. The four different

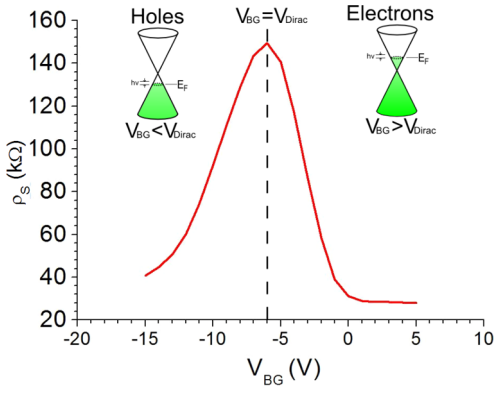

Figure 2. Graphene sheet resistivity between source and drain of the a = 22 μm split-ring array, measured at different back-gate voltages. The CNP is observed at a back-gate bias of −6 V, yielding a maximum resistance of 150 kΩ, which is compatible with top-gated[22] n-doped graphene. Different arrays exhibit similar plots with slightly different CNPs and ρ_s^{max} corresponding to biases between −6 and −4 V, characteristic of n-doped graphene.

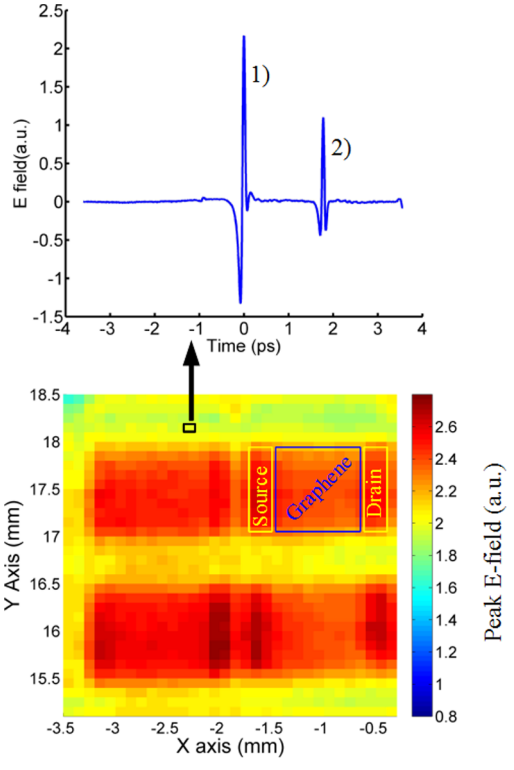

Figure 3. Maximum *E*-field signal reflected, recorded at different sample positions. The sample was kept in the focus of the system, and the minimum linear step size corresponds to 100 μm. Each pixel corresponds, as shown in the inset, to a complex waveform. It is possible to clearly distinguish (1) the reflection from the first surface and (2) a second reflection from the bottom surface.

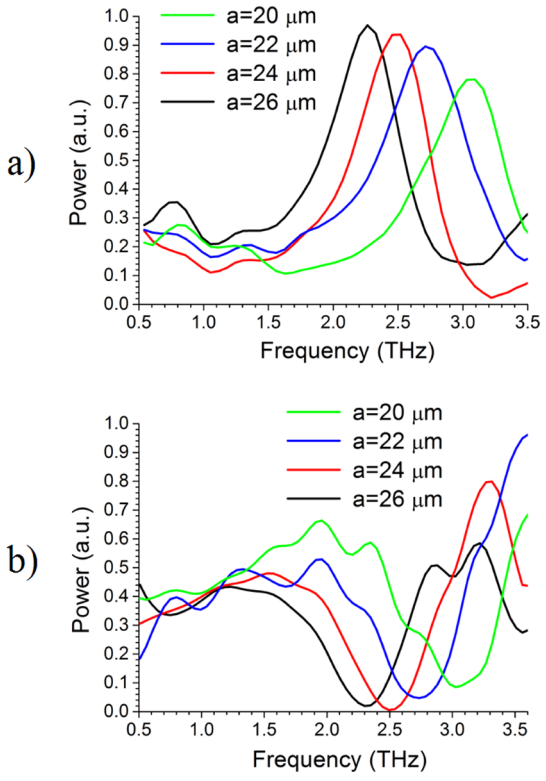

Figure 4. Normalized reflection from the top (a) and back (b) sample surfaces from the different split-ring arrays. The back-reflection from the sample is proportional to the transmission through the SRR arrays. Different arrays are identified by the split-ring side length *a* and present resonances between 2.25 and 3.1 THz, with a lithographic tuning of ~250 GHz, in good agreement with the simulations.

split-rings arrays are distinguishable together with the source and drain metallic pads. Each pixel yields, as shown in Figure 3, the reflected *E*-field, composed of two pulses corresponding to (1) the reflection from the sample front surface and (2) the reflection from the back surface. Since these two waveforms are quite distinct, truncation would not result in a significant loss of information. After having operated a fast Fourier transform on each reflection, we obtained two spectra. One obtained from the first pulse corresponds to the reflection, while the second one is proportional to the transmission from the split-ring arrays. The spectrum proportional to transmission is noiser, due to the multiple reflections and weaker signal-to-noise ratio. Figure 4 presents the normalized (to a signal reflected from a metallic feature) power corresponding to the top (a) and back (b) reflected waveforms similar to (1) and (2) of Figure 3. All these measurements have been recorded by keeping $V_{TG} = V_{BG} = 0$. The different arrays, identified by the square side length *a*, present broad resonances varying from 2.25 to 3.1 THz, thus covering the sweet frequency spot of QCLs, with a fwhm of ~500 GHz, separated by ~250 GHz, in good agreement with the simulations. Although the back-reflected signals are noiser, because of the roughness of the back surface, as well as reflections from the interfaces of different material layers, a remarkable match was observed between the minimum values proportional to the transmission and the peaks arising from the top reflection. The reflection curves presented in Figure 4 are representative of each array. It is worth stressing again that the THz spot of ~200 μm was illuminating an area covered by about $5 \times 5 \rightarrow 7 \times 7$ SR elements (corresponding to a = 26 μm → 20 μm). Therefore, from the measurements of Figure 3 we could infer the electromagnetic response of ~25 independent areas, within the single 1×1 mm^2 pattern. Those measurements exhibit resonances that differ within 100 GHz, yielding a reproducibility that is larger than the frequency shift observed in the other patterns with different *a* value. These resonances were identified as the LC resonances of the split rings, arising from the cancellation of the currents passing through the inductive arms of the split rings and having the maximum electric field enhancement in the capacitor gap. The so-called *dipole* resonance, characterized by having the maximum in the inductive part of the split rings, lies outside of the spectral content of the THz pulses. By rotating the polarization by 90° (rotating the sample) and performing similar measurements, we did not observe any resonances, as expected, since the only resonance mode (*dipole*) that could be excited with this polarization lies outside of the frequency range monitored. Changing the major carrier concentration of the graphene along the Dirac cone and depleting the charges below the split rings indirectly yields an active control over the optical intensity of the incident light, because of the overlap between the graphene and the plasmonic mode of the resonant elements. The measurements presented in Figure 2 are fundamental since they not only give us insight into the doping of the graphene monolayer but also provide us with a picture of the voltage-induced changes in the major carrier concentration. In fact, such a characterization cannot be achieved by biasing the top gate (top contact/SRR arrays), since it cannot yield a uniform voltage-induced charge modification over the whole graphene area. Furthermore, the reproducibility of the plot presented in Figure 2 was considered a measure of the stability of the graphene monolayer during all the measurements. A voltage span of about 20 V was needed in order to clearly identify the Dirac point (approximately corresponding to −5 V) and to observe a change in the sign of the major carriers in the graphene monolayer, when biasing the graphene from the back gate through the p-doped Si substrate and a 300 nm thick SiO_2 layer. Therefore, when biasing the device with a top gate where the buffering layer is ~35 nm, a voltage span of 2 V was applied, and a maximum peak intensity, corresponding to the CNP of the graphene layer, is expected around −0.5 V bias. Indeed, that was experimentally observed when the split-ring arrays were biased, thus acting as top gate,

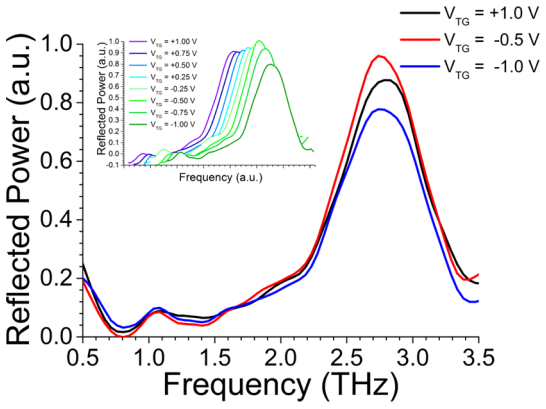

Figure 5. Reflected intensity from the split-ring arrays with $a = 22\ \mu$m, having a peak frequency at 2.7 THz, at different top-gate biases. The reflection peak is at maximum for a negative bias voltage of −0.5 V, consistent with the initial doping calculated from the CNP point presented in Figure 2. The reflected intensities measured at all the bias voltages are presented in the inset, in a waterfall arrangement for clarity.

with respect to the graphene layer, while keeping $V_{BG} = 0$. In this nonoptimized device, a maximum modulation depth of ∼18% was achieved, as shown in Figure 5 for the $a = 22\ \mu$m array reporting at reflected peak resonance for the three different voltages of 1 V (n-doping), −0.5 V (Dirac point), and −1 V (p-doping). The whole set of waveforms corresponding to the different biases has been reported for completeness in the inset, arranged in waterfall by introducing an offset in frequency for each curve. Because the voltage-induced change in the carrier density is not uniform over the entire graphene surface, but is concentrated in the split-ring area, the modulation is mostly effective at the resonant frequency and only marginally noticeable elsewhere, thus yielding a clean and well-defined response. More details of the measured modulation depths achieved for the different arrays are reported in Table 1.

The modulation depths measured were reduced for SRR arrays with a larger a value, having also a larger capacitive gap, because the voltage-induced change in the carrier concentration in graphene was less effective. Moreover, it should be mentioned that, due to the variability in the quality of the graphene sheet below, which was differently affected by the fabrication process, the bias response of the SRR was not uniform over the whole array surface. In fact, by calculating the sheet conductivities as a function of the back-gate voltages for the arrays different from the one with a central frequency at 2.7 THz, Dirac points similar to the one shown in Figure 2 were found, but characterized by a lower contrast in the conductivity plot and wider peak features, attributed to the lower uniformity and thus responsivity of the graphene material below. Differently from ref 18, since the SRR elements are not directly in contact with the graphene monolayer,

TABLE 1. Modulation Depths for Different SRR Arrays[a]

split-ring array (a, μm)	max modulation depth (n-doping)	max modulation depth (p-doping)
20	6%	10%
22	8%	18%
24	8%	8%
26	6%	7%

[a] Measured maximum modulation depths for different arrays obtained by biasing the sample through the top-gate: the modulation depth observed is maximum for the array $a = 22\ \mu$m. All these values have an indetermination of 1%.

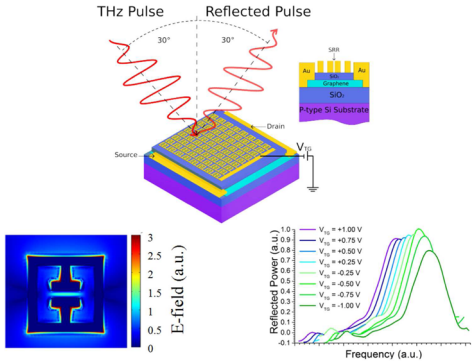

Figure 6. Maximum modulation depths measured and simulated from the split-ring arrays with $a = 22\ \mu$m, yielding the values of 18% and 30%, respectively.

the modulation effect is due to the overlap between the plasmonic optical mode in the split ring and the graphene. Thus, a theoretical analysis cannot be performed by using a direct analogy with a transmission-line model based on a simple electrical circuit, and thus it requires a finite-element model of the whole graphene/SRR system.

In order to better analyze our experimental data, a simulation using Comsol Multiphysics investigated the power reflected from the THz light incident on a single split-ring resonator, while varying the conductivity σ_{intra} of the graphene layer.

$$\sigma_{intra} = -i\frac{e^2 k_B T}{\pi\hbar^2(\omega - 1/\tau)}\left(\frac{E_F}{k_B T} + 2\ln(e^{-E_F/k_B T} + 1)\right) \quad (1)$$

This was accomplished by using the Kubo formula[23] and considering only the intraband absorption, as presented in eq 1, where ω represents the incident frequency, k_B the Boltzmann constant, T the experimental temperature condition, E_F the Fermi energy, and finally τ the scattering time. The last two values are the only unknown parameters in the formula, since all the experiments were carried out at room temperature, and from the measurements presented in Figure 2 we could infer the Fermi energy, by using a similar procedure to the one presented in ref 18. We assumed for the scattering time a fixed value of 15 fs.[24] Figure 6 presents a comparison between the modulation depth already

reported in Figure 5 and the maximum modulation depth achievable from the simulations by inserting eq 1. The two curves are in good agreement, with the measured profiles red-shifted by only 150 GHz. The maximum modulation depth simulated is 30% and is obtained assuming a sheet conductivity $\sigma_s = 0$ at the CNP. The discrepancy between measured and simulated values is attributed to the finite conductivity observed at the Dirac point. In fact, from the measurements presented in Figure 2 we could infer the values of σ_s at the CNP and with the unbiased sample, $\sigma_s = 6.67E^{-6}$ S and $\sigma_s = 5E^{-5}$ S, respectively, which yielded a simulated modulation depth of about 12%, in good agreement with the experimental values. The maximum modulation depth achieved is in good agreement with the values reported in ref 18 but, due to the top-gate architecture, achieved with a much lower bias of ~0.5 V instead of the 10.6 V reported. The bias voltage required to drive these amplitude modulators is about 60 times lower when compared to the values reported in ref 14, where a modulation depth of 64% was achieved. Moreover, our approach is based on a bidimensional architecture, independent of the substrate thickness, thus offering the capability to design a device working at different frequencies. Finally, the implementation of a back-gate, for changing the graphene properties globally, combined with a top-gate, in order to modify the graphene properties locally, yields a high flexibility in the operation of such devices and opens the way to a wide range of applications.

CONCLUSIONS

In conclusion, we have presented the realization of a lithographically tunable optical modulator, based on split-ring resonator arrays and graphene. The advantage over similar devices is the ultralow bias of less than 0.5 V. This ultralow bias corresponds to a maximum modulation depth, in this nonoptimized device, of 18%. The modulation depth achieved could be further improved, *i.e.*, by multiple monolayer graphene depositions and lowering the bias required. The split-ring resonances have been clearly identified and observed in reflection measurements. Furthermore, our integrated device, consisting of different arrays, completely covers the frequency region between 2 and 3 THz. This is the region where QCLs strongly emit, thus being ready to be implemented with such sources for external amplitude/phase modulation experiments.

METHODS

Sample Fabrication. Sample fabrication starts from monolayer graphene grown by CVD. Graphene growth by CVD was performed on Cu foils (25 μm thick, Alfa Aesar purity 99.999%) using C_6H_6 as the precursor. After CVD the graphene was transferred to Si/SiO_2 (300 nm) wafers using a PMMA support layer (poly(methyl methacrylate) 495 diluted to 2% in anisole) and $FeCl_3$ to etch the Cu. Further details on this can be found elsewhere.[25,26] We patterned the graphene sample into an array of squares each with an area of 1 mm^2, using optical lithography and oxygen dry etching. The source (S) and drain (D) metal pads covering both the individual graphene areas and the SiO_2 substrate (as presented in Figure 1a) were defined by optical lithography, Ti/Au (10/80 nm) evaporation, and lift-off. Then, we spun hydrogen silsesquioxane FOX-12 resin from Dow Corning mixed with methyl isobutyl ketone in equal parts on the whole surface. After thermal curing at 350 °C in a N_2 atmosphere, it yielded a 35 nm oxide buffering layer. On top of the samples we realized, *via* e-beam lithography followed by Ti/Au (10/100 nm) metal deposition and lift off, arrays of split rings with different dimensions, all having different frequency resonances. The resulting arrays of split rings that cover a range of resonance frequencies are all located on the same device, each sitting atop individual graphene areas. A further lithographic step followed by HF wet etching is required for the removal of the oxide layer from the source/drain metal pads for wire bonding. All the split rings in every single array are connected to one another, with the connecting lines having a negligible effect on the reflection properties.[3]

Conflict of Interest: The authors declare no competing financial interest.

Acknowledgment. R.D., D.S.J., Y.D.S., H.E.B., and D.A.R. acknowledge EPSRC for financial support. S.H. acknowledges funding from EPSRC under grant GRAPHTED (project reference EP/K016636/1).

REFERENCES AND NOTES

1. Tonouchi, M. Cutting-Edge Terahertz Technology. *Nat. Photonics* **2007**, *1*, 97–105.
2. Bao, Q.; Loh, K. P. Graphene Photonics, Plasmonics, and Broadband Optoelectronic Devices. *ACS Nano* **2012**, *6*, 3677–3694.
3. Chen, H.-T.; Padilla, W. L.; Zide, J. M. O.; Gossard, A. C.; Taylor, A. J.; Averitt, R. Active Terahertz Metamaterial Device. *Nature* **2006**, *444*, 597–600.
4. Chen, H.-T.; Padilla, W. L.; Cich, M. J.; Azad, A. K.; Averitt, R.; Taylor, A. J. A Metamaterial Solid-State Terahertz Phase Modulator. *Nat. Photonics* **2009**, *3*, 148–151.
5. Tao, H.; Padilla, W. J.; Zhang, X.; Averitt, R. D. Recent Progress in Electromagnetic Metamaterial Devices for Terahertz Applications. *IEEE J. Sel. Top. Quantum Electron.* **2011**, *17*, 92–101.
6. Avouris, P. Graphene: Electronic and Photonic Properties and Devices. *Nano Lett.* **2010**, *10*, 4285–4294.
7. Tredicucci, A.; Vitiello, M. S. Device Concepts for Graphene-Based Terahertz Photonics. *IEEE J. Sel. Top. Quantum Electron.* **2014**, *20*, 8500109.
8. Castro Neto, A. H.; Guinea, F.; Peres, N. M. R.; Novoselov, K. S.; Geim, A. K. The Electronic Properties of Graphene. *Rev. Mod. Phys.* **2009**, *81*, 109–162.
9. Echtermeyer, T. J.; Britnell, L.; Jasnos, P. K.; Lombardo, A.; Gorbachev, R. V.; Grigorenko, A. N.; Geim, A. K.; Ferrari, A. C.; Novoselov, K. S. Strong Plasmonic Enhancement of Photovoltage in Graphene. *Nat. Commun.* **2011**, *2*, 458.
10. Ju, L.; Geng, B.; Horng, J.; Girit, C.; Martin, M.; Hao, Z.; Bechtel, H. A; Liang, X.; Zettl, A.; Shen, Y. R.; *et al.* Graphene Plasmonics for Tunable Terahertz Metamaterial. *Nat. Nanotechnol.* **2011**, *6*, 630–634.
11. Basko, D. A Photothermal Effect in Graphene. *Science* **2011**, *334*, 610–611.
12. Yan, J.; Kim, M.-H.; Elle, J. A.; Sushkov, A. B.; Jenkins, G. S.; Milchberg, H. M.; Fuhrer, M. S.; Drew, H. D. Dual-Gated

Bilayer Graphene Hot-Electron Bolometer. *Nat. Nanotechnol.* **2012**, *7*, 472–478.
13. Grigorenko, A. N.; Polini, M.; Novoselov, K. S. Graphene Plasmonics. *Nat. Photonics* **2012**, *6*, 749–758.
14. Sensale-Rodriguez, B.; Yan, R.; Kelly, M. M.; Fang, T.; Tahy, K.; Hwang, W. S.; Jena, D.; Liu, L.; Xing, H. G. Broadband Graphene Terahertz Modulators Enabled by Intraband Transitions. *Nat. Commun.* **2012**, *3*, 780.
15. Sensale-Rodriguez, B.; Yan, R.; Rafique, S.; Zhu, M.; Li, W.; Liang, X.; Gundlach, D.; Protasenko, V.; Kelly, M. M.; Jena, D.; *et al*. Extraordinary Control of Terahertz Beam Reflectance in Graphene Electro-Absorption Modulators. *Nano Lett.* **2012**, *12*, 4518–4522.
16. Yan, R.; Sensale-Rodriguez, B.; Liu, L.; Jena, D.; Xing, H. G. A New Class of Electrically Tunable Metamaterial Terahertz Modulators. *Opt. Express* **2013**, *21*, 2324–2330.
17. Vasic, B.; Jakovljevic, M. M.; Isic, G.; Gajic, R. Tunable Metamaterial Based on Split Rings Resonators and Doped Graphene. *Appl. Phys. Lett.* **2013**, *103*, 011102.
18. Valmorra, F.; Scalari, G.; Maissen, C.; Fu, W.; Schoenenberger, C.; Choi, J. W.; Park, H. G.; Beck, M.; Faist, J. Low-Bias Active Control of Terahertz Waves by Coupling Large-Area CVD Graphene to a Terahertz Metamaterial. *Nano Lett.* **2013**, *13*, 3193–3198.
19. Pi, K.; McCreary, M.; Bao, W.; Han, W.; Chiang, Y. F.; Li, Y.; Tsai, S.-W.; Lau, C. N.; Kawakami, R. K. Electronic Doping and Scattering by Transition Metals on Graphene. *Phys. Rev. B* **2009**, *80*, 075406.
20. Brenner, K.; Murali, R. Single Step, Complementary Doping of Graphene. *Appl. Phys. Lett.* **2010**, *96*, 063104.
21. Shen, Y.-C.; Taday, P. F. Development and Application of Terahertz Pulsed Imaging for Nondestructive Inspection of Pharmaceutical Tablet. *IEEE J. Sel. Top. Quantum Electron.* **2008**, *14*, 407–415.
22. Lemme, M. C.; Echtermeyer, T. J.; Baus, M.; Szafranek, B. N.; Bolten, J.; Schmidt, M.; Wahlbrink, T.; Kurz, H. Mobility in Graphene Double Gate Field Effect Transistors. *Solid-State Electron.* **2008**, *52*, 514–518.
23. Gusynin, V. P.; Sharapov, S. G.; Carbotte, J. P. On the Universal Ac Optical Background in Graphene. *New J. Phys.* **2009**, *11*, 095013.
24. Lee, S. H.; Choi, M.; Kim, T.-T.; Lee, S.; Liu, M.; Yin, X.; Choi, H. K.; Lee, S.; Choi, C.-G.; Choi, S.-Y.; *et al*. Switching Terahertz Waves with Gate-Controlled Active Graphene Metamaterials. *Nat. Mater.* **2012**, *11*, 936–941.
25. Kidambi, P. R.; Ducati, C.; Dlubak, B.; Gardiner, D.; Weatherup, R. S.; Martin, M.-B.; Seneor, P.; Coles, H.; Hofmann, S. The Parameter Space of Graphene Chemical Vapor Deposition on Polycrystalline Cu. *J. Phys. Chem. C* **2012**, *116*, 22492–22501.
26. Kidambi, P. R.; Bayer, B. C.; Blume, R.; Wang, Z.-J.; Baehtz, C.; Weatherup, R. S; Willinger, M.-G.; Schloegl, R.; Hofmann, S. Observing Graphene Grow: Catalyst Graphene Interactions during Scalable Graphene Growth on Polycristalline Copper. *Nano Lett.* **2013**, *13*, 4769–4778.